

## Electronic Effects Determine the Selectivity of Planar Au-Cu Bimetallic Thin Films for Electrochemical CO<sub>2</sub> Reduction

Liu, Kai; Ma, Ming; Wu, Longfei; Valenti, Marco; Cardenas-Morcoso, Drialys; Hofmann, Jan P.; Bisquert, Juan; Gimenez, Sixto; Smith, Wilson A.

**DOI**

[10.1021/acsami.9b01553](https://doi.org/10.1021/acsami.9b01553)

**Publication date**

2019

**Document Version**

Final published version

**Published in**

ACS Applied Materials and Interfaces

**Citation (APA)**

Liu, K., Ma, M., Wu, L., Valenti, M., Cardenas-Morcoso, D., Hofmann, J. P., Bisquert, J., Gimenez, S., & Smith, W. A. (2019). Electronic Effects Determine the Selectivity of Planar Au-Cu Bimetallic Thin Films for Electrochemical CO<sub>2</sub> Reduction. *ACS Applied Materials and Interfaces*, 11(18), 16546-16555. <https://doi.org/10.1021/acsami.9b01553>

**Important note**

To cite this publication, please use the final published version (if applicable). Please check the document version above.

**Copyright**

Other than for strictly personal use, it is not permitted to download, forward or distribute the text or part of it, without the consent of the author(s) and/or copyright holder(s), unless the work is under an open content license such as Creative Commons.

**Takedown policy**

Please contact us and provide details if you believe this document breaches copyrights. We will remove access to the work immediately and investigate your claim.

# Electronic Effects Determine the Selectivity of Planar Au–Cu Bimetallic Thin Films for Electrochemical CO<sub>2</sub> Reduction

Kai Liu,<sup>†</sup> Ming Ma,<sup>†</sup> Longfei Wu,<sup>‡</sup> Marco Valenti,<sup>†</sup> Drialys Cardenas-Morcoso,<sup>§</sup> Jan P. Hofmann,<sup>‡</sup> Juan Bisquert,<sup>§</sup> Sixto Gimenez,<sup>§</sup> and Wilson A. Smith<sup>\*,†</sup>

<sup>†</sup>Materials for Energy Conversion and Storage (MECS), Department of Chemical Engineering, Faculty of Applied Sciences, Delft University of Technology, Van der Maasweg 9, 2629 HZ Delft, The Netherlands

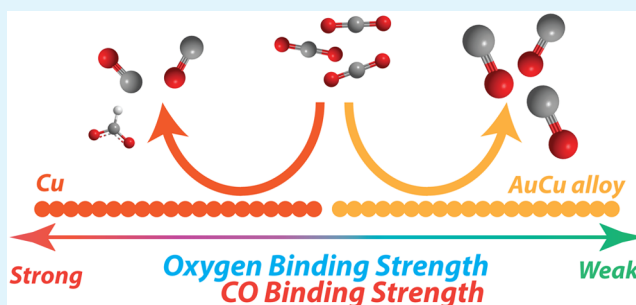
<sup>‡</sup>Laboratory for Inorganic Materials and Catalysis (IMC), Department of Chemical Engineering and Chemistry, Eindhoven University of Technology, P.O. Box 513, 5600 MB Eindhoven, The Netherlands

<sup>§</sup>Institute of Advanced Materials (INAM), Universitat Jaume I, Avenida de Vicent Sos Baynat, s/n, 12006 Castelló de la Plana, Spain

## Supporting Information

**ABSTRACT:** Au–Cu bimetallic thin films with controlled composition were fabricated by magnetron sputtering co-deposition, and their performance for the electrocatalytic reduction of CO<sub>2</sub> was investigated. The uniform planar morphology served as a platform to evaluate the electronic effect isolated from morphological effects while minimizing geometric contributions. The catalytic selectivity and activity of Au–Cu alloys was found to be correlated with the variation of electronic structure that was varied with tunable composition. Notably, the d-band center gradually shifted away from the Fermi level with increasing Au atomic ratio, leading to a weakened binding energy of \*CO, which is consistent with low CO coverage observed in CO stripping experiments. The decrease in the \*CO binding strength results in the enhanced catalytic activity for CO formation with the increase in Au content. In addition, it was observed that copper oxide/hydroxide species are less stable on Au–Cu surfaces compared to those on the pure Cu surface, where the surface oxophilicity could be critical to tuning the binding strength of \*OCHO. These results imply that the altered electronic structure could explain the decreased formation of HCOO<sup>−</sup> on the Au–Cu alloys. In general, the formation of CO and HCOO<sup>−</sup> as main CO<sub>2</sub> reduction products on planar Au–Cu alloys followed the shift of the d-band center, which indicates that the electronic effect is the major governing factor for the electrocatalytic activity of CO<sub>2</sub> reduction on Au–Cu bimetallic thin films.

**KEYWORDS:** electrochemical carbon dioxide reduction, bimetallic catalyst, Au–Cu alloy, thin film, electronic effect, d-band center



## 1. INTRODUCTION

The electrocatalytic reduction of CO<sub>2</sub> is a promising way to sustainably convert CO<sub>2</sub> into high-value added products, chemicals, and fuels. A large amount of materials have been examined theoretically and experimentally as electrocatalysts for the CO<sub>2</sub> reduction reaction (CO<sub>2</sub>RR) under various conditions.<sup>1–8</sup> These studies show that the CO<sub>2</sub> reduction activity and selectivity of transition-metal catalysts is fundamentally limited by a linear scaling relationship between reaction intermediates.<sup>9</sup> Among a wide variety of well-studied metallic catalysts for CO<sub>2</sub>RR, Au and Cu are very attractive, as Au has shown the highest activity for the selective production of CO,<sup>5</sup> and Cu has the largest range of product selectivities with the ability to form up to 16 different products.<sup>10</sup> While the activity of these transition metals has improved steadily in the past few years due to the increased global research efforts, their optimal performance is still hindered by the scaling relationship.<sup>11</sup> Recently, it has been proposed that alloying two metals (or making bimetallic electrodes) is an efficient

approach to promote the improved activity and selectivity of the electroreduction of CO<sub>2</sub> by tuning the binding strength of intermediates with a modified electronic structure.<sup>5,6,12</sup> It has been found that tuning the composition of bimetallic/alloy materials can offer a simple way to effectively change the local electronic structure of the composite materials, which also has beneficial properties to create new binding sites at the interface of the two metals with different binding energies than the linearly extrapolated values of each individual metals.<sup>13,14</sup>

Au–Cu bimetallic alloys have been previously investigated for electrochemical CO<sub>2</sub>RR and shown remarkable performance.<sup>14</sup> However, recent works on bimetallic catalysts (including Au–Cu) have focused on nanostructured catalysts, which complicates mechanistic understanding due to the combined effects of both the metal composition/electronic

Received: January 24, 2019

Accepted: April 10, 2019

Published: April 10, 2019

structure and the surface morphology,<sup>8,14–16</sup> which affects mass transport of reactants and products near the surface and leads to different surface coverages. A high turnover rate was observed on Au<sub>3</sub>Cu bimetallic nanoparticles, and the enhanced activity for CO formation on Au–Cu bimetallic nanoparticles was attributed to the synergistic geometric and electronic effects.<sup>8,14</sup> From the view of thermodynamics, the electronic effect results from the variation in the electronic structure, which can tune the binding strength of intermediates and even be able to provide new binding sites, for example, optimizing the binding strength of the \*CO and \*COOH intermediates.<sup>13,17</sup> However, the geometric effect can control the kinetics of a reaction, as the morphology can affect the mass transport, which may alter the interfacial reaction conditions.<sup>18,19</sup> Based on the published results,<sup>7,14</sup> there is still a lack of comprehensive understanding of these effects or a potential synergistic effect, as the geometric and electronic effects simultaneously participate in CO<sub>2</sub>RR on nanocatalysts, and it is difficult to distinguish the actual role of the electronic structure and morphology individually. Therefore, it is important to decouple these phenomena and investigate the relative influences of each effect.

Other Au-based alloys (most notably, Au–Pt<sup>20</sup> and Au–Pd<sup>21</sup>) have also been explored for CO<sub>2</sub>RR. Au is near the peak of the Sabatier volcano plot for CO formation, while Pt and Pd bind very strongly to CO. The catalytic behavior of Au–Pt alloys for CO formation acts as expected from the relationship and follows a linear scaling relationship between \*COOH and \*CO binding energies. On the other hand, in the volcano plot of HCOO<sup>−</sup>, Au, Pt, and Pd all show a weak binding energy to \*OCHO and are far away from the volcano peak. However, alloys of Au–Pt can produce upward of 5% faradaic efficiency of HCOO<sup>−</sup>.<sup>20</sup> This result is ascribed to the synergistic effect derived from alloying, where new binding sites apart from Au and Pt can form a favorable pathway to produce HCOO<sup>−</sup>. Cu is also on the weak binding side of the volcano plot for the formation of HCOO<sup>−</sup>, having an intermediate binding strength of \*OCHO and lower \*H binding energy than Pt and Pd. However, the formation of HCOO<sup>−</sup> on Au–Cu alloys in the kinetic-limited potential region is rarely discussed. A systematic and detailed investigation of the activity and selectivity for HCOO<sup>−</sup> formation on Au–Cu alloys will therefore be useful for researchers to obtain a more complete understanding of the electronic effects of these alloys on their product selectivity.

In this work, we fabricated Au–Cu bimetallic thin films by magnetron sputtering, which offers a flexible way to make compositionally variant thin films that are dense and relatively flat, giving an ideal platform to investigate the compositional/electronic effects without having a nanostructured surface, which may affect mass transport and local variations of reaction conditions. A systematic experimental investigation was applied to this planar bimetallic platform to quantitatively compare the intrinsic activity of the catalysts as a function of Au and Cu composition. With X-ray diffraction (XRD) and electrochemical impedance spectroscopy (EIS) characterization, it was possible to find a relationship between grain size, charge-transfer resistance, and microstrain to understand the reactivity of the catalysts. Combining these results with CO stripping measurements, we found that as the content of Au rises, the desorption energy of \*CO decreases, and therefore the release of CO becomes more efficient. The weakened oxygen binding strength on Au–Cu alloys is revealed by CV measurements, which leads to the low binding strength of

oxygen-bonded \*OCHO and further reduces the formation of HCOO<sup>−</sup>. Given the variety of physical and electronic characteristics studied in these Au–Cu bimetallic films, it seems that the d-band energy is the most important factor that influences the reactivity of the bimetallic films. Insights gained from this well-defined system will help to understand the variation of intermediate binding strength due to the local electronic effect and further develop high-performance catalysts with desired selectivity and activity.

## 2. EXPERIMENTAL SECTION

**2.1. Preparation of Au–Cu Bimetallic Thin Films by Magnetron Sputtering.** The bimetallic thin films were fabricated by a previously published co-deposition method.<sup>20</sup> Briefly, the magnetron sputtering targets of Au (99.99%, MaTeck GmbH) and Cu (99.99%, MaTeck GmbH) are powered by radio frequency (RF) and direct current (DC) generators, respectively. The deposition power and duration were precisely controlled to obtain films with a desired thickness (80 nm) and composition ratios on Ti foil substrates.

**2.2. Morphological Investigation.** The large-scale morphology was investigated under a scanning electron microscope (SEM, JEOL JSM-6010LA). The surface roughness was characterized by atomic force microscopy (AFM, Bruker).

**2.3. Structural Characterization.** The crystal structure of bimetallic thin films were characterized by X-ray diffraction (XRD) using a diffractometer (Bruker D8 Discover). The bulk composition was determined by energy-dispersive X-ray spectroscopy (EDS, JEOL JSM-6010LA). X-ray photoelectron spectroscopy (XPS, Thermo Scientific K-Alpha) was conducted to confirm the composition on the surface.

**2.4. Electrochemical Measurements.** Electrochemical measurements were carried out in a two-compartment home-made cell. The cathode and anode components were separated by an anion exchange membrane (AEM, Fumasep FAB-PK-130). Electrochemical impedance spectroscopy (EIS) was carried out under the same conditions as CO<sub>2</sub> reduction. CO stripping was conducted in the same cell. Briefly, a 0.1 M KHCO<sub>3</sub> electrolyte was bubbled with Ar for 15 min with vigorous stirring. All the samples were pre-reduced by holding a potential at −0.2 V vs RHE for 100 s to ensure the surface was metallic and no residual oxides were present on the surface. CO adsorption was performed at 0.1 V vs RHE with purging CO for 15 min; meanwhile, the absorbed H was released. Prior to CO stripping, the electrolyte was bubbled with Ar for 20 min to remove the excessive dissolved CO. The scan range of CO stripping was from 0 to +1.5 V vs RHE at a scan rate of 50 mV/s.

**2.5. Catalytic Performance.** The gaseous products were analyzed by gas chromatography (GC, Interscience). The cathodic compartment was sparged with CO<sub>2</sub> at a constant flow rate, and the outlet was directly connected to a gas chromatograph. Liquid products of the CO<sub>2</sub>RR were collected and quantified by <sup>1</sup>H nuclear magnetic resonance (NMR, Agilent) after the electrolysis.

## 3. RESULTS AND DISCUSSION

**3.1. Morphological Investigation of the Au–Cu Bimetallic Thin Films Deposited on Ti Substrates.** Magnetron sputtering deposition offers a highly reproducible process to fabricate high purity Au–Cu bimetallic films, as the deposition is performed in a vacuum chamber with controlled Argon pressure. With the co-deposition of Au and Cu, the deposition rates of the two materials can be tuned by adjusting the sputtering powers of Au and Cu targets, thus precisely controlling the atomic ratio of binary films.<sup>20</sup> The surface of the films was first investigated by SEM. From the SEM images (seen in Figure S1), it is shown that the 80 nm-thick metallic films with different compositions exhibit a relatively uniform surface, suggesting that the as-prepared planar surface is ideal

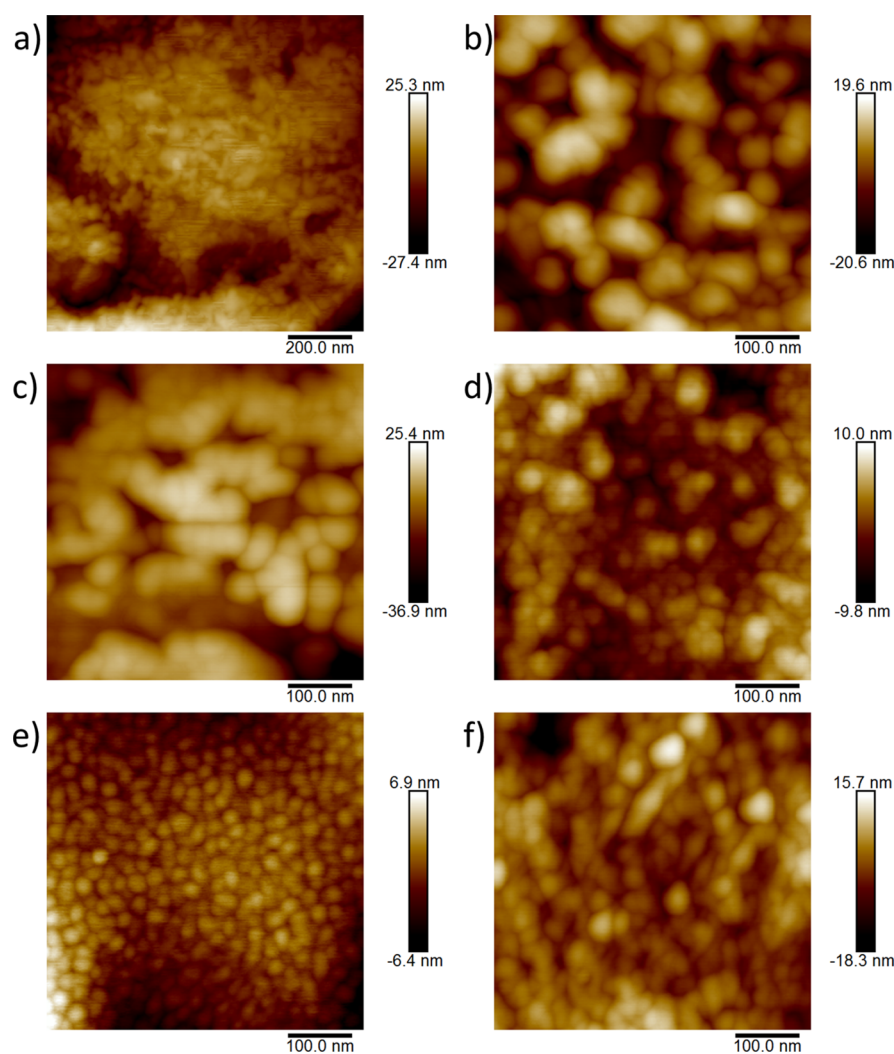


**Figure 1.** AFM images of (a) bare Ti foils and catalyst films after CO<sub>2</sub>RR at  $-0.7$  V vs RHE for 1 h: (b) Au, (c) Au<sub>75</sub>Cu<sub>25</sub>, (d) Au<sub>50</sub>Cu<sub>50</sub>, (e) Au<sub>25</sub>Cu<sub>75</sub>, and (f) Cu thin film.

for reducing the impact of local pH effects associated with nanostructured or mesostructured morphologies and provides a consistent platform across all the film compositions.<sup>22</sup>

To better understand the local structure of the thin films, AFM was carried out on the films deposited on Ti foils, with the results shown in Figure 1 and Figure S2. The surface of sputtered thin films have a relatively smooth and uniform morphology, which is typical for sputtered metallic thin films that are expected to be formed through vertical columnar growth.<sup>23–25</sup> The relative deposition powers of Au and Cu were adjusted to achieve the desired compositional ratio, while the surface roughness was not significantly varied (as shown in Table S1), which demonstrates that the morphology is not affected by the different fabrication conditions. As presented in Figure S2, in this work, there is no evident nanostructuring or further roughening of the surface introduced by the deposition, which ensures that the CO<sub>2</sub>RR activity would not be influenced by the variation of surface roughness and local mass transport. In addition, the surface was examined after CO<sub>2</sub>RR experiments, which shows a similar morphology, indicating that the surface structure remained constant during electrolysis (seen in Figure 1). The double-layer capacitance ( $C_{dl}$ ) was measured to evaluate the relative electrochemically active surface area (ECSA) and surface roughness. As

shown in Figure S3, all the capacitances of the as-prepared samples possess a similar value compared to those of flat Au and Cu foils with a smooth surface, revealing that the as-prepared films exhibit a low surface roughness and have a relative uniform distribution of active sites.<sup>26</sup>

**3.2. Structural Characterization of the Au–Cu Binary Catalytic Films.** In order to obtain an accurate stoichiometric ratio, the molar volume of Au (10.21 cm<sup>3</sup>/mol) and Cu (7.124 cm<sup>3</sup>/mol) were taken into consideration while the magnetron sputtering deposition was performed, such that the obtained films could contain a desired composition and have the same thickness. The crystal structure of the as-prepared films was examined by XRD, with the results shown in Figure 2. The XRD patterns show that all the sputtered samples have one dominant characteristic, which is assigned to the diffraction of the (111) plane from the face-centered cubic (FCC) crystal structure. As shown in the patterns, the position of the dominant peak gradually shifts from 44° to 50.7° as the stoichiometric ratio of Cu is increased, and no characteristic peak of pure Au or Cu was observed in the co-deposited samples, which demonstrates that Au and Cu are alloyed with each other rather than being randomly physically mixed or phase-separated.

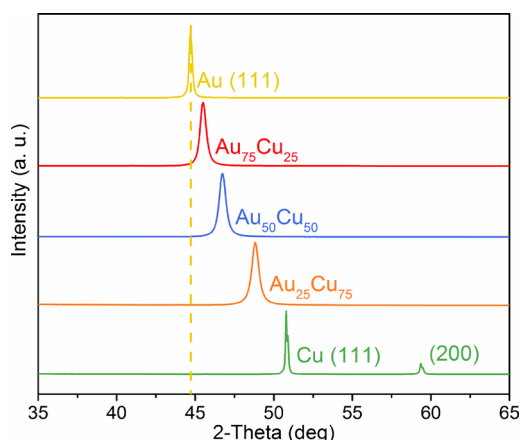


**Figure 2.** XRD patterns of the binary metallic films with varied compositions.

The as-deposited thin films were characterized by EDS and XPS to investigate the bulk and surface atomic ratio, with the results shown in Figure 3. It can be seen that the surface and

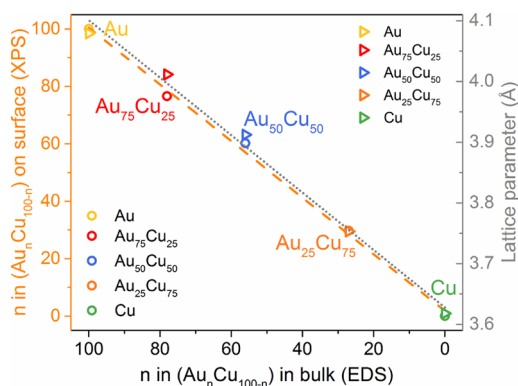


**Figure 3.** Comparison of the surface composition with bulk composition (ring open) and variation of lattice parameters of the as-prepared samples (triangle right-pointing open). The dashed orange line provides a general guide to the trend of data points (slope: 0.9860,  $R^2 = 0.9957$ ). The dotted black line presents the prediction of Vegard's law based on the lattice parameters of Au and Cu ( $R^2 = 0.9891$ ).

bulk composition are in agreement with each other, representing that there is no obvious phase segregation near the surface and the stoichiometric ratio is identical from the bulk to the surface. Besides the uniform composition, the increase in lattice parameter is linear with the rise of Au content (shown in Figure 3), suggesting that the uniform atomic arrangement is stable across the varied compositions and indicating that the formation of Au–Cu alloys is validated by Vegard's law.<sup>27</sup>

To further analyze the effect of the crystallite structure, the structural parameters of the binary thin-film electrodes were extracted from the XRD data and are summarized in Table 1. It can be seen that the difference in the radius of Au (166 pm) and Cu (140 pm) atoms leads to the microstrain in the bimetallic thin films. It has been reported that grain boundaries play a vital role on the activity of CO<sub>2</sub>RR and the grain boundary density increases as the grain size becomes smaller.<sup>28–30</sup> Therefore, it is relevant to investigate the grain size as a function of binary composition. The grain size of the

**Table 1.** Structural Metrics of As-Deposited Electrodes

sample	grain size (nm)	microstrain (%)
Au	27.49	0.0039
Au <sub>75</sub> Cu <sub>25</sub>	19.00	0.0055
Au <sub>50</sub> Cu <sub>50</sub>	17.37	0.0058
Au <sub>25</sub> Cu <sub>75</sub>	16.24	0.0060
Cu	33.68	0.0028

alloy thin films are similar to each other (represented in Table 1) and much smaller than the grain size of the pure Au and Cu films. The microstrain in the alloy samples is higher than that in the individual Au and Cu films, which is consistent with a previous report.<sup>31</sup> This result is expected since there is more strain with multicomponent films than with a single atomic component.

In addition to the crystalline and morphological properties of the alloy thin films, the electronic structure can also play an important role in CO<sub>2</sub>RR. By varying the electronic structure of transition metals, the interaction between the adsorbates and d-band electronic structure can be tuned, which can in turn alter the binding strength of intermediates.<sup>14</sup> The surface valence band XPS measurements were conducted to investigate the energy variation of d-orbital electrons. However, copper can immediately react with oxygen, forming a thin oxide layer even with short exposure to air. Additionally, the surface adsorbates could also introduce some electronic state, influencing the valence band spectral region and the d-band center determination.<sup>32</sup> Thus, depth profile XPS was conducted to understand the effects of the native oxide and adsorbates on the d-band center. As the oxidation layer is very thin and no obvious adsorbate-induced peak was found in the valence band integration region, the d-band center seems to not be affected by the thin surface oxide layer (seen in Figure S5 and Table S2). As presented in Figure 4, surface valence bands of the Au–Cu bimetallic catalysts exhibit different patterns compared to those of Au or Cu, and the center of the d-band gradually shifts away from the Fermi level as the Au content increases. This d-band shift can affect the occupancy of antibonding states, which in turn suggests that the binding strength for intermediates is weakened.<sup>14,33</sup> XPS measurements were performed before and after electrolysis, showing the same overall trend of the d-orbital electron, and no new features or phase segregations occurred after performing CO<sub>2</sub> reduction (seen in Figures S7 and S8).

### 3.3. Electrochemical Properties of the As-Prepared Thin Films.

The Au–Cu bimetallic catalysts were characterized by cyclic voltammetry (CV) in an alkaline solution to investigate the electrochemical properties of Cu, Au, and alloys of the two metals. The sputtered Au thin films exhibited similar reduction features (shown in Figure 5a) as reported previously.<sup>34</sup> The oxidation and reduction peaks of Cu are clearly shown in Figure 5e. In the oxidation region of Cu, peak 1 indicates the formation of Cu<sub>2</sub>O.<sup>35</sup> As the potential increased positively, the Cu-containing film subsequently starts to form Cu(OH)<sub>2</sub> (indicated as peak 2).<sup>36,37</sup> Under more anodic potentials, another broad oxidation peak starts to appear (peak 3), implying the formation of a duplex surface film consisted of an inner Cu<sub>2</sub>O layer and an outer CuO/Cu(OH)<sub>2</sub> layer.<sup>36,37</sup> In the reduction process, two obvious reduction peaks correspond to the Cu(II)-to-Cu(I) and Cu(I)-to-Cu(0) reduction reactions, which are denoted as peak 4 and peak 5, respectively.<sup>37</sup> To obtain a more comprehensive understanding

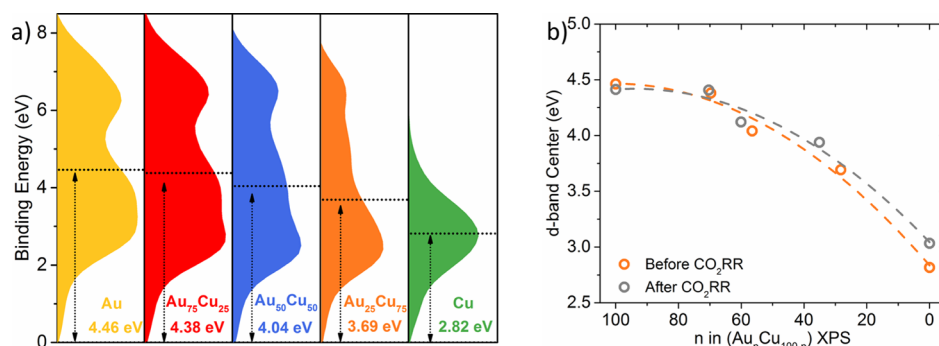


**Figure 4.** Surface valence band X-ray photoemission spectra of the as-prepared Au, Cu, and Au–Cu alloys. (a) As-prepared samples before CO<sub>2</sub>RR and (b) the d-band center of these samples before and after CO<sub>2</sub>RR at –0.7 V vs RHE for 1 h. The gravity center of the valence band center is shown by the dotted lines compared to 0 eV. The binding energy is the value of  $|E - E_{\text{Fermi}}|$ .

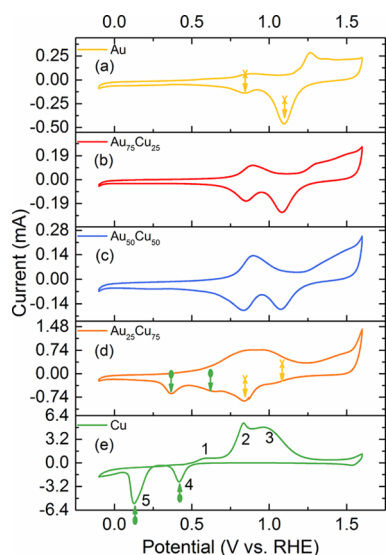


**Figure 5.** Cyclic voltammograms of sputtered catalysts in N<sub>2</sub>-saturated 0.5 M KOH at a scan rate of 50 mV/s: (a) Au, (b) Au<sub>75</sub>Cu<sub>25</sub>, (c) Au<sub>50</sub>Cu<sub>50</sub>, (d) Au<sub>25</sub>Cu<sub>75</sub>, and (e) Cu. The reduction peaks of copper oxides species are marked by green arrows with dots. The reduction waves of gold are marked by yellow arrows with crosses.

of the Cu oxidation process, a further study was performed in the less anodic region (as shown in Figure S9). From the results, it can be seen that the Cu oxidation is suppressed, indicating that the neighboring Au atoms potentially inhibit this oxidation process,<sup>38</sup> and the oxidation peak of Cu is slightly positively shifted, suggesting that the oxygen binding is weakened on Au–Cu alloys due to the d-band center shifting away from the Fermi level.<sup>39</sup>

As the sputtered samples exhibit an almost identical planar morphology, the effect due to the adsorption/desorption of electrolyte species on the precise evaluation of interfacial capacitance can be extracted from electrochemical impedance spectroscopy (EIS).<sup>40</sup> For CO<sub>2</sub>RR, it can be assumed that the imaginary component of the impedance ( $Z''$ ) represents the dynamic adsorption process occurring at the interface. The surface coverage is extracted from EIS following a previously published method.<sup>41</sup> When the electrode surface is fully covered by the analyte, this imaginary component of the impedance is denoted as  $Z''_{\text{max}}$ . The  $Z''$  induced by faradaic adsorption of reactant species is denoted as  $Z''_{\text{ads}}$ . The surface coverage percentage is determined by the ratio of  $Z''_{\text{ads}}$  to

$Z''_{\text{max}}$ .<sup>41</sup> As shown in Figure 6, the descending trend of the surface coverage as a function of applied potentials over all the samples demonstrates the fast reaction kinetics under high overpotentials.<sup>41</sup>

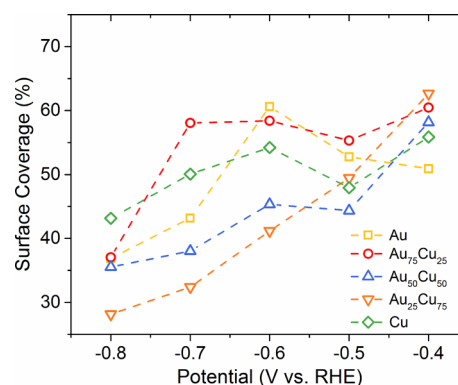


**Figure 6.** Potential-dependent surface coverage of faradaic adsorption extracted from EIS data.

Facile charge-transfer kinetic is observed by EIS with negatively increased potentials. As gold has a relatively lower onset potential than copper, the charge-transfer resistance ( $R_{\text{ct}}$ ) on Au is lower than that on Cu in the low potential region ( $< -0.3$  V vs RHE). Also, the  $R_{\text{ct}}$  value of Au–Cu alloys was decreased in the less negative potential region with increasing Au content (seen in Figure 7a). When the overpotential is high enough to efficiently prompt the CO<sub>2</sub>RR, the difference in  $R_{\text{ct}}$  between the electrodes shrinks rapidly, indicating that a significant kinetical improvement in HER and CO<sub>2</sub>RR is driven by the applied potentials. The detailed plots of charge-transfer resistance as a function of composition and applied potential are shown in Figure S13. As the lattice strain at the surface could influence the binding strength of intermediates reducing the overall energy barrier,<sup>29</sup> the relationship between the microstrain and charge-transfer resistance is presented in Figure 7b. It is clearly shown that the low charge-transfer resistance is in line with the high microstrain, which implies that the microstrain derived from grain boundaries could promote the overall electrochemical kinetics. This direct correlation between the microstrain and charge-transfer resistance gives important insights into the significance of the surface electronic properties of thin films, adsorption of reactant molecules, and kinetics of electrocatalysis.

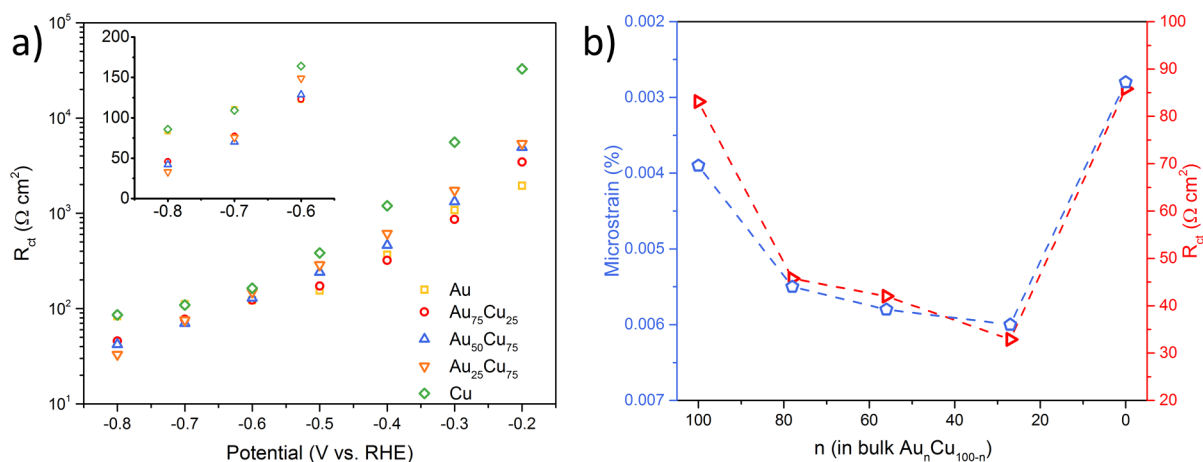


**Figure 7.** Comparison of charge-transfer resistance. (a) Charge-transfer resistance of bimetallic thin films in the potential range of  $-0.2$  to  $-0.8$  V vs RHE. Inset: a zoom-in image of the potential region of  $-0.6$  to  $-0.8$  V vs RHE. (b) Relationship between the microstrain derived from XRD data and charge-transfer resistance (at  $-0.8$  V vs RHE) extracted from EIS.

The adsorbed CO is a key intermediate for  $\text{CO}_2\text{RR}$ , and Cu has an intermediate binding strength for  $^*\text{CO}$ , allowing the formation of  $\text{C}_2$  or  $\text{C}_3$  products, while Au owns the optimum binding strength for  $^*\text{COOH}$  and  $^*\text{CO}$ , prompting the conversion from  $\text{CO}_2$  to  $\text{CO}$ .<sup>5</sup> CO stripping experiments could elucidate the variation of CO binding strength introduced by the change of electronic structure and the amount of active sites by calculating the amount of absorbed-desorbed CO. As summarized in Table 2, the CO coverage was

**Table 2.** CO Coverage Determined by CO Stripping

samples	CO oxidation charge ( $\mu\text{C}$ )	CO coverage ( $\text{nmol}^{-1} \text{ cm}^{-2}$ )
Au	4.9	0.13
$\text{Au}_{75}\text{Cu}_{25}$	13.0	0.34
$\text{Au}_{50}\text{Cu}_{50}$	10.0	0.26
$\text{Au}_{25}\text{Cu}_{75}$	13.4	0.35
Cu	24.2	0.63

dramatically reduced even with a small content of Au, revealing that Au can significantly lower the desorption energy of CO and decrease the population of surface-bound CO, which is consistent with the large d-band center shift from pure Cu to  $\text{Au}_{25}\text{Cu}_{75}$  (seen in Figure 4).

**3.4. Electrocatalytic Performance of Au–Cu Bimetallic Thin Films for  $\text{CO}_2\text{RR}$ .** In the investigated potential region, no hydrocarbons were detected, as only  $\text{H}_2$ , CO, and

$\text{HCOO}^-$  were found, indicating that the activation energy is not high enough or the concentration of hydrocarbons is below the detection limit of the gas chromatography.<sup>42</sup> The  $\text{FE}_{\text{CO}}$  scales with the composition and applied potential (seen in Figure 8a), as the more negative potential can provide higher activation energy for  $\text{CO}_2\text{RR}$ , and the higher Au content can decrease the  $^*\text{COOH}$  formation energy and lower  $^*\text{CO}$  binding energy, which selectively makes the formation of CO more favorable.<sup>14</sup> As it is proposed that either the stronger or weaker oxygen binding on Cu sites could be able to optimize the binding strength of  $^*\text{COOH}$  on Au–Cu interfaces,<sup>13,16</sup> however, no obvious enhancement is observed here, which could be ascribed to the significantly weakened  $^*\text{CO}$  binding.<sup>8</sup> On the other hand, the formation of  $\text{HCOO}^-$  was strongly suppressed with the introduction of Au (seen in Figure 8b). This dramatic suppression can be ascribed to the significantly weakened oxygen binding strength as the d-band center shifts away from the Fermi level with the increasing Au content, which limits the formation of  $^*\text{OCHO}$ .<sup>3</sup> As the  $\text{CO}_2\text{RR}$  requires higher activation energy than HER,<sup>43</sup> there is no obvious inhibition of HER in the thin films under low overpotentials. In the high overpotential region, the HER on high Au-content catalysts is inhibited (Figure 8c), which is due to the improved  $\text{CO}_2\text{RR}$  activity in bimetallic samples with increased Au content and the more favorable binding of  $\text{CO}_2\text{RR}$  intermediates on Au–Cu alloys.<sup>44,45</sup>

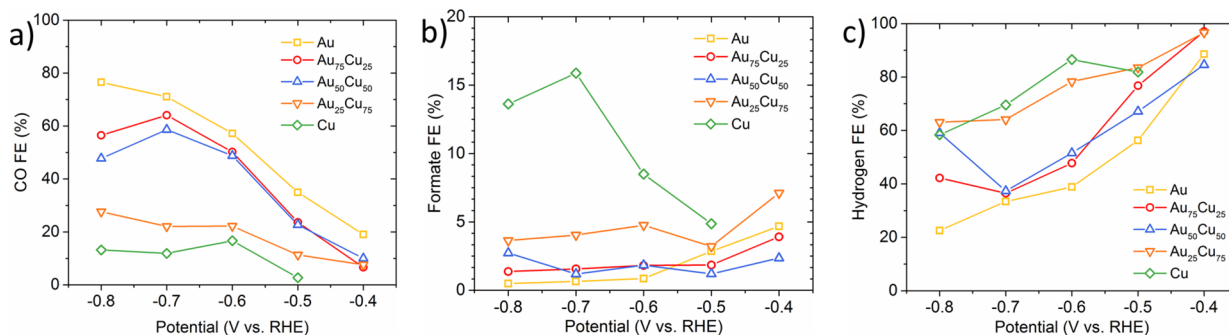


**Figure 8.** Comparison of the electrocatalytic performance for  $\text{CO}_2$  reduction. Faradaic efficiency of (a) CO, (b)  $\text{HCOO}^-$ , and (c)  $\text{H}_2$  with varied potentials and compositions.

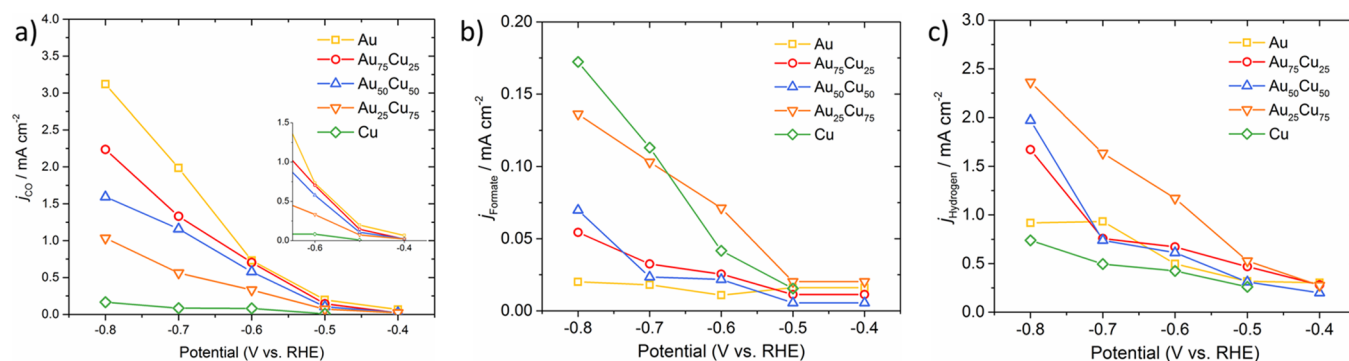


**Figure 9.** Activity of bimetallic catalysts for two-electron products. Partial current densities of (a) CO, (b)  $\text{HCOO}^-$ , and (c)  $\text{H}_2$  are shown as a function of applied potentials. Inset: a zoom-in image of the potential region of  $-0.4$  to  $-0.6$  V vs RHE.

The total current density of all samples was found to increase steadily as the applied potential raised negatively (seen in Figure S14). The partial current density of CO was correspondingly enhanced with the increase in Au content, indicating that the activity for CO production is strongly influenced by the presence of Au, which can lower the activation energy of  $\text{CO}_2\text{RR}$  and reduce the desorption energy of  $^*\text{CO}$  accelerating the CO production. Based on the analysis of CO formation, it is clearly shown that the catalytic activity for CO formation is almost linear with the increase in Au content, which demonstrates that the CO generation rate follows the shift of the d-band center, such that the d-band theory seems to be the dominant factor affecting the activity and selectivity for CO in this planar Au–Cu bimetallic system (seen in Figure 4).

The  $\text{CO}_2\text{RR}$  and hydrogen evolution reaction not only compete but also interact with each other. The surface-bound  $\text{CO}_2\text{RR}$  species may impede HER, and the  $^*\text{H}$  binding energy could be altered by the surface-adsorbed species.<sup>44,46</sup> Notably, although Cu has an intermediate binding strength of CO, the activity of HER is not significantly affected by the introduction of Au to Cu across the investigated potential region (seen in Figure 9c), which is due to the fact that Au and Cu exhibit a similar activity in the HER volcano plot with the presence of  $\text{CO}_2$ .<sup>46</sup> It is important to note that the HER activity is not inhibited by alloying on Au–Cu bimetallic surfaces, revealing that the improved selectivity to CO resulted from the enhanced activity for CO on Au–Cu alloys instead of the suppression of HER.

The  $\text{Au}_{25}\text{Cu}_{75}$  film exhibits a relatively higher HER activity than the other samples, which may be due to the surface atomic rearrangement taking place when the applied potential is above  $-0.6$  V vs RHE, resulting in the surface Au content increasing to 35% (seen in Table S2). This instability is consistent with simulation results.<sup>47</sup> In Au–Fe nanoparticles, it was observed that the Fe atoms leach out, leaving more Au active sites on the surface that can prompt the production of CO.<sup>48</sup> Notwithstanding, the surface rearrangement introducing more surface Au atoms, the  $j_{\text{CO}}$  value still falls in line with the shift of the d-band center derived from the variation of composition. The surface rearrangement on  $\text{Au}_{25}\text{Cu}_{75}$  shows no obvious contribution to the CO production; on the contrary, it suggests that the CO activity is governed by the bulk electronic structure. The  $\text{H}_2$  current density on  $\text{Au}_{25}\text{Cu}_{75}$  is strongly elevated as the applied potential was increased more negatively, which implies that the surface reconstruction exposes more active sites for HER. As presented in Figure 6,

the surface coverage on  $\text{Au}_{25}\text{Cu}_{75}$  declines rapidly with the negatively increasing potential, which can be attributed to the improved HER. Moreover, even though the bimetallic catalysts contain more microstrain (seen in Table 1), the performance of these Au–Cu alloy samples still follows the ascending trend in CO formation with the increase in Au content, which implies that the bulk electronic effect on Au–Cu for CO production is the governing effect over the additional Au active sites and microstrain.

It is reported that Au could increase the CO concentration near the surface and elevate the local pH by enhanced water splitting and these conditions may facilitate the formation of  $\text{C}_2/\text{C}_{2+}$  products on Cu surfaces.<sup>26,49</sup> Notwithstanding, there are no detectable  $\text{C}_2$  products on the planar Au–Cu alloys; instead, the selectivity to formate is dramatically inhibited along with the prompted evolution of CO with the increasing Au content (seen in Figure 8), suggesting that the formation of formate is unlikely to follow the reaction pathway through the  $^*\text{COOH}$  intermediate on the binary Au–Cu metallic thin films.<sup>50</sup> The current density of formate declines rapidly as the Au content increases (seen in Figure 9); yet, there is no obvious linear relationship between the composition and activity, especially in the potential region that the overpotential is relatively high and the  $\text{CO}_2$  mass transport limitation is minimized, for example,  $-0.7$  and  $-0.6$  V vs RHE. These observations could be ascribed to (i) the variation in  $^*\text{OCHO}$  binding energy has a strong influence on  $\text{HCOO}^-$  production, for example, a much faster declining trend in  $\text{HCOO}^-$  formation. In the volcano plots of CO and  $\text{HCOO}^-$ , the difference in  $j_{\text{CO}}$  between Cu and Au is around one order of magnitude; however, the difference in  $j_{\text{formate}}$  is around two orders of magnitude;<sup>3</sup> (ii) the enhanced HER on  $\text{Au}_{25}\text{Cu}_{75}$  could facilitate the formation of  $\text{HCOO}^-$  by prompting the proton transfer to  $^*\text{OCHO}$ . As observed in the CV scans (seen in Figure 5), the positively shifted reduction peak of copper oxide/hydroxide species may suggest the lowered oxygen affinity on the surface, which also relates to the low oxophilicity of the alloy, possibly resulting in a weakened binding of oxygen-bonded  $^*\text{OCHO}$ .<sup>3,39</sup> It has been confirmed that, on Au–Pt and Au–Pd, the activity of CO formation is consistent with the Au composition, which demonstrates that the  $^*\text{COOH}$  binding strength is tuned by the electronic effect as the d-band center shifts along with the variation of Au content. On the other hand, these two kinds of Au-based alloys exhibit an enhanced activity for  $\text{HCOO}^-$  formation.<sup>20,21</sup> However, on planar binary Au–Cu thin films, the varied electronic structure with increased Au content seems to be able to not only

promote CO formation by lowering the formation energy of \*COOH and reducing the desorption energy of \*CO but could also suppress the production of HCOO<sup>-</sup> via decreasing the binding affinity of \*OCHO to the low activity region. In addition, by comparing the relative position of Cu and Pt in the volcano plot of HCOO<sup>-</sup>, it can be found that Pt has an even lower \*OCHO binding energy than Cu, implying that the averaged \*OCHO binding strength of Au and Pt seems unlikely to play a dominant role to improve the selectivity to HCOO<sup>-</sup>. Considering both Pt and Pd are strong \*CO and optimum \*H binding metals, the effect of surface adsorbates on HCOO<sup>-</sup> formation and the proton transfer for HCOO<sup>-</sup> production may be worth further exploring.

#### 4. CONCLUSIONS

In this work, uniformly deposited Au–Cu bimetallic films with controlled composition were explored as a platform to study the isolated electronic effect and remove the effects of nano/mesostructuring for CO<sub>2</sub> electroreduction. The introduction of Au can significantly reshape the d-band electronic structure and notably weakens the binding strength of \*CO. Similar to the planar Au–Pt alloys, the d-band electronic structure of Au–Cu alloys can be tuned by varying the composition to adjust the \*CO binding energy in these bimetallic systems. The activity and selectivity for the reduction of CO<sub>2</sub> to CO was gradually improved with increasing Au content, revealing that the electronic effect itself cannot solely break the linear scaling relationship without nanostructure engineering. Nevertheless, the copper oxide/hydroxide species on Au–Cu surfaces were less stable than those on pure copper, indicating that the introduction of Au could also lower the binding strength between copper and oxygen on the alloy surface. As the surface oxophilicity could be critical to the formation of HCOO<sup>-</sup>, alloying Cu with Au can decrease the adsorption energy of \*OCHO, thus inhibiting the formation of HCOO<sup>-</sup>. The electronic effect/d-band structure could strongly influence the formation of HCOO<sup>-</sup>; however, the activity of HCOO<sup>-</sup> does not scale with the compositional shift. Considering Cu has an intermediate \*CO binding and relatively low \*H binding energy compared to Pt and Pd, the nonlinear correlation between  $j_{\text{formate}}$  and composition requires more theoretical effort to investigate the relationship between composition, structure, and selectivity.

#### ■ ASSOCIATED CONTENT

##### Supporting Information

The Supporting Information is available free of charge on the ACS Publications website at DOI: 10.1021/acsami.9b01553.

Structural characterizations including XRD, AFM, XPS, and EDS; double-layer capacitance; Auger and depth profile XPS; valence band XPS; cyclic voltammetry; CO stripping; Bode and Nyquist plots; and charge-transfer resistance (PDF)

#### ■ AUTHOR INFORMATION

##### Corresponding Author

\*E-mail: W.Smith@tudelft.nl.

##### ORCID

Ming Ma: 0000-0003-3561-5710

Jan P. Hofmann: 0000-0002-5765-1096

Wilson A. Smith: 0000-0001-7757-5281

#### Notes

The authors declare no competing financial interest.

#### ■ ACKNOWLEDGMENTS

This work is supported by the China Scholarship Council (CSC, No. 201507565007) and a VIDU grant awarded to W.A.S. from the Netherlands Organization for Scientific Research (NWO). The authors would like to thank Prof. Bernard Dam and Dr. Recep Kas for helpful discussions. We would also like to thank Riming Wang for his assistance in the product characterization. Joost Middelkoop and Herman Schreuders are acknowledged for helping with designing the CO<sub>2</sub> electrochemical cell and sputtering deposition, respectively.

#### ■ REFERENCES

- (1) Kuhl, K. P.; Hatsukade, T.; Cave, E. R.; Abram, D. N.; Kibsgaard, J.; Jaramillo, T. F. Electrocatalytic Conversion of Carbon Dioxide to Methane and Methanol on Transition Metal Surfaces. *J. Am. Chem. Soc.* **2014**, *136*, 14107–14113.
- (2) Resasco, J.; Chen, L. D.; Clark, E.; Tsai, C.; Hahn, C.; Jaramillo, T. F.; Chan, K.; Bell, A. T. Promoter Effects of Alkali Metal Cations on the Electrochemical Reduction of Carbon Dioxide. *J. Am. Chem. Soc.* **2017**, *139*, 11277–11287.
- (3) Feaster, J. T.; Shi, C.; Cave, E. R.; Hatsukade, T.; Abram, D. N.; Kuhl, K. P.; Hahn, C.; Nørskov, J. K.; Jaramillo, T. F. Understanding Selectivity for the Electrochemical Reduction of Carbon Dioxide to Formic Acid and Carbon Monoxide on Metal Electrodes. *ACS Catal.* **2017**, *7*, 4822–4827.
- (4) Singh, M. R.; Kwon, Y.; Lum, Y.; Ager, J. W., III; Bell, A. T. Hydrolysis of Electrolyte Cations Enhances the Electrochemical Reduction of CO<sub>2</sub> over Ag and Cu. *J. Am. Chem. Soc.* **2016**, *138*, 13006–13012.
- (5) Hansen, H. A.; Varley, J. B.; Peterson, A. A.; Nørskov, J. K. Understanding Trends in the Electrocatalytic Activity of Metals and Enzymes for CO<sub>2</sub> Reduction to CO. *J. Phys. Chem. Lett.* **2013**, *4*, 388–392.
- (6) Peterson, A. A.; Nørskov, J. K. Activity Descriptors for CO<sub>2</sub> Electroreduction to Methane on Transition-Metal Catalysts. *J. Phys. Chem. Lett.* **2012**, *3*, 251–258.
- (7) Mistry, H.; Reske, R.; Strasser, P.; Roldan Cuenya, B. Size-Dependent Reactivity of Gold-Copper Bimetallic Nanoparticles during CO<sub>2</sub> Electroreduction. *Catal. Today* **2017**, *288*, 30–36.
- (8) Kim, D.; Xie, C.; Becknell, N.; Yu, Y.; Karamad, M.; Chan, K.; Crumlin, E. J.; Nørskov, J. K.; Yang, P. Electrochemical Activation of CO<sub>2</sub> through Atomic Ordering Transformations of AuCu Nanoparticles. *J. Am. Chem. Soc.* **2017**, *139*, 8329–8336.
- (9) Hong, X.; Chan, K.; Tsai, C.; Nørskov, J. K. How Doped MoS<sub>2</sub> Breaks Transition-Metal Scaling Relations for CO<sub>2</sub> Electrochemical Reduction. *ACS Catal.* **2016**, *6*, 4428–4437.
- (10) Kuhl, K. P.; Cave, E. R.; Abram, D. N.; Jaramillo, T. F. New Insights into the Electrochemical Reduction of Carbon Dioxide on Metallic Copper Surfaces. *Energy Environ. Sci.* **2012**, *5*, 7050–7059.
- (11) Chan, K.; Tsai, C.; Hansen, H. A.; Nørskov, J. K. Molybdenum Sulfides and Selenides as Possible Electrocatalysts for CO<sub>2</sub> Reduction. *ChemCatChem* **2014**, *6*, 1899–1905.
- (12) Higgins, D.; Landers, A. T.; Ji, Y.; Nitopi, S.; Morales-Guio, C. G.; Wang, L.; Chan, K.; Hahn, C.; Jaramillo, T. F. Guiding Electrochemical Carbon Dioxide Reduction toward Carbonyls Using Copper Silver Thin Films with Interphase Miscibility. *ACS Energy Lett.* **2018**, 2947–2955.
- (13) Back, S.; Kim, J.-H.; Kim, Y.-T.; Jung, Y. Bifunctional Interface of Au and Cu for Improved CO<sub>2</sub> Electroreduction. *ACS Appl. Mater. Interfaces* **2016**, *8*, 23022–23027.
- (14) Kim, D.; Resasco, J.; Yu, Y.; Asiri, A. M.; Yang, P. Synergistic geometric and electronic effects for electrochemical reduction of

carbon dioxide using gold–copper bimetallic nanoparticles. *Nat. Commun.* **2014**, *5*, 4948.

(15) Ross, M. B.; Dinh, C. T.; Li, Y.; Kim, D.; De Luna, P.; Sargent, E. H.; Yang, P. Tunable Cu Enrichment Enables Designer Syngas Electrosynthesis from CO<sub>2</sub>. *J. Am. Chem. Soc.* **2017**, *139*, 9359–9363.

(16) Andrews, E.; Fang, Y.; Flake, J. Electrochemical reduction of CO<sub>2</sub> at CuAu nanoparticles: size and alloy effects. *J. Appl. Electrochem.* **2018**, *48*, 435–441.

(17) Chang, Z.; Huo, S.; Zhang, W.; Fang, J.; Wang, H. The Tunable and Highly Selective Reduction Products on Ag@Cu Bimetallic Catalysts Toward CO<sub>2</sub> Electrochemical Reduction Reaction. *J. Phys. Chem. C* **2017**, *121*, 11368–11379.

(18) Ma, M.; Trzeźniewski, B. J.; Xie, J.; Smith, W. A. Selective and Efficient Reduction of Carbon Dioxide to Carbon Monoxide on Oxide-Derived Nanostructured Silver Electrocatalysts. *Angew. Chem. Int. Ed.* **2016**, *55*, 9748–9752.

(19) Yoon, Y.; Hall, A. S.; Surendranath, Y. Tuning of Silver Catalyst Mesostructure Promotes Selective Carbon Dioxide Conversion into Fuels. *Angew. Chem. Int. Ed.* **2016**, *55*, 15282–15286.

(20) Ma, M.; Hansen, H. A.; Valenti, M.; Wang, Z.; Cao, A.; Dong, M.; Smith, W. A. Electrochemical Reduction of CO<sub>2</sub> on Compositionally Variant Au–Pt Bimetallic Thin Films. *Nano Energy* **2017**, *42*, 51–57.

(21) Hahn, C.; Abram, D. N.; Hansen, H. A.; Hatsukade, T.; Jackson, A.; Johnson, N. C.; Hellstern, T. R.; Kuhl, K. P.; Cave, E. R.; Feaster, J. T.; Jaramillo, T. F. Synthesis of thin film AuPd alloys and their investigation for electrocatalytic CO<sub>2</sub> reduction. *J. Mater. Chem. A* **2015**, *3*, 20185–20194.

(22) Ma, M.; Djanashvili, K.; Smith, W. A. Controllable Hydrocarbon Formation from the Electrochemical Reduction of CO<sub>2</sub> over Cu Nanowire Arrays. *Angew. Chem. Int. Ed.* **2016**, *55*, 6680–6684.

(23) Peters, T. A.; Kaleta, T.; Stange, M.; Bredesen, R. Development of Thin Binary and Ternary Pd-Based Alloy Membranes for Use in Hydrogen Production. *J. Membr. Sci.* **2011**, *383*, 124–134.

(24) Smith, W.; Fakhouri, H.; Pulpytel, J.; Mori, S.; Grilli, R.; Baker, M. A.; Arefi-Khonsari, F. Visible Light Water Splitting via Oxidized TiN Thin Films. *J. Phys. Chem. C* **2012**, *116*, 15855–15866.

(25) Thornton, J. A. Influence of Apparatus Geometry and Deposition Conditions on the Structure and Topography of Thick Sputtered Coatings. *J. Vac. Sci. Technol.* **1974**, *11*, 666–670.

(26) Morales-Guio, C. G.; Cave, E. R.; Nitopi, S. A.; Feaster, J. T.; Wang, L.; Kuhl, K. P.; Jackson, A.; Johnson, N. C.; Abram, D. N.; Hatsukade, T.; Hahn, C.; Jaramillo, T. F. Improved CO<sub>2</sub> Reduction Activity towards C<sub>2+</sub> Alcohols on a Tandem Gold on Copper Electrocatalyst. *Nat. Catal.* **2018**, *1*, 764–771.

(27) Chang, F.; Shan, S.; Petkov, V.; Skeete, Z.; Lu, A.; Ravid, J.; Wu, J.; Luo, J.; Yu, G.; Ren, Y.; Zhong, C.-J. Composition Tunability and (111)-Dominant Facets of Ultrathin Platinum–Gold Alloy Nanowires toward Enhanced Electrocatalysis. *J. Am. Chem. Soc.* **2016**, *138*, 12166–12175.

(28) Feng, X.; Jiang, K.; Fan, S.; Kanan, M. W. Grain-Boundary-Dependent CO<sub>2</sub> Electroreduction Activity. *J. Am. Chem. Soc.* **2015**, *137*, 4606–4609.

(29) Mariano, R. G.; McKelvey, K.; White, H. S.; Kanan, M. W. Selective Increase in CO<sub>2</sub> Electroreduction Activity at Grain-Boundary Surface Terminations. *Science* **2017**, *358*, 1187–1192.

(30) Feng, X.; Jiang, K.; Fan, S.; Kanan, M. W. A Direct Grain-Boundary-Activity Correlation for CO Electroreduction on Cu Nanoparticles. *ACS Cent. Sci.* **2016**, *2*, 169–174.

(31) Rosenberg, Y.; Machavariani, V. S.; Voronel, A.; Garber, S.; Rubenstein, A.; Frenkel, A. I.; Stern, E. A. Strain Energy Density in the X-Ray powder Diffraction from Mixed Crystals and Alloys. *J. Phys.: Condens. Matter* **2000**, *12*, 8081–8088.

(32) Hofmann, T.; Yu, T. H.; Folse, M.; Weinhardt, L.; Bär, M.; Zhang, Y.; Merinov, B. V.; Myers, D. J.; Goddard, W. A., III; Heske, C. Using Photoelectron Spectroscopy and Quantum Mechanics to Determine d-Band Energies of Metals for Catalytic Applications. *J. Phys. Chem. C* **2012**, *116*, 24016–24026.

(33) Nørskov, J. K.; Bligaard, T.; Rossmeisl, J.; Christensen, C. H. Towards the computational design of solid catalysts. *Nat. Chem.* **2009**, *1*, 37–46.

(34) Tominaga, M.; Shimazoe, T.; Nagashima, M.; Kusuda, H.; Kubo, A.; Kuwahara, Y.; Taniguchi, I. Electrocatalytic Oxidation of Glucose at Gold–Silver Alloy, Silver and Gold Nanoparticles in an Alkaline Solution. *J. Electroanal. Chem.* **2006**, *590*, 37–46.

(35) Kunze, J.; Maurice, V.; Klein, L. H.; Strehblow, H.-H.; Marcus, P. In Situ Scanning Tunneling Microscopy Study of the Anodic Oxidation of Cu(111) in 0.1 M NaOH. *J. Phys. Chem. B* **2001**, *105*, 4263–4269.

(36) Kunze, J.; Maurice, V.; Klein, L. H.; Strehblow, H.-H.; Marcus, P. In Situ STM Study of the Duplex Passive Films Formed on Cu(111) and Cu(001) in 0.1 M NaOH. *Corros. Sci.* **2004**, *46*, 245–264.

(37) Maurice, V.; Strehblow, H.-H.; Marcus, P. In Situ STM Study of the Initial Stages of Oxidation of Cu(111) in Aqueous Solution. *Surf. Sci.* **2000**, *458*, 185–194.

(38) Higgins, D.; Wette, M.; Gibbons, B. M.; Siahrostami, S.; Hahn, C.; Escudero-Escribano, M.; García-Melchor, M.; Uliassi, Z.; Davis, R. C.; Mehta, A.; Clemens, B. M.; Nørskov, J. K.; Jaramillo, T. F. Copper Silver Thin Films with Metastable Miscibility for Oxygen Reduction Electrocatalysis in Alkaline Electrolytes. *ACS Appl. Energy Mater.* **2018**, 1990–1999.

(39) Okada, M.; Tsuda, Y.; Oka, K.; Kojima, K.; Diño, W. A.; Yoshigoe, A.; Kasai, H. Experimental and Theoretical Studies on Oxidation of Cu–Au Alloy Surfaces: Effect of Bulk Au Concentration. *Sci. Rep.* **2016**, *6*, 31101.

(40) Shrikrishnan, S.; Sankaran, K.; Lakshminarayanan, V. Electrochemical Impedance Analysis of Adsorption and Enzyme Kinetics of Calf Intestine Alkaline Phosphatase on SAM-Modified Gold Electrode. *J. Phys. Chem. C* **2012**, *116*, 16030–16037.

(41) Shah, A. H.; Wang, Y.; Woldu, A. R.; Lin, L.; Iqbal, M.; Cahen, D.; He, T. Revisiting Electrochemical Reduction of CO<sub>2</sub> on Cu Electrode: Where Do We Stand about the Intermediates? *J. Phys. Chem. C* **2018**, *122*, 18528–18536.

(42) Monzó, J.; Malewski, Y.; Kortlever, R.; Vidal-Iglesias, F. J.; Solla-Gullón, J.; Koper, M. T. M.; Rodriguez, P. Enhanced Electrocatalytic Activity of Au@Cu Core@Shell Nanoparticles towards CO<sub>2</sub> Reduction. *J. Mater. Chem. A* **2015**, *3*, 23690–23698.

(43) Martín, A. J.; Larrázabal, G. O.; Pérez-Ramírez, J. Towards Sustainable Fuels and Chemicals through the Electrochemical Reduction of CO<sub>2</sub>: Lessons from Water Electrolysis. *Green Chem.* **2015**, *17*, 5114–5130.

(44) Ooka, H.; Figueiredo, M. C.; Koper, M. T. M. Competition between Hydrogen Evolution and Carbon Dioxide Reduction on Copper Electrodes in Mildly Acidic Media. *Langmuir* **2017**, *33*, 9307–9313.

(45) Lee, S.; Park, G.; Lee, J. Importance of Ag–Cu Biphasic Boundaries for Selective Electrochemical Reduction of CO<sub>2</sub> to Ethanol. *ACS Catal.* **2017**, *7*, 8594–8604.

(46) Cave, E. R.; Shi, C.; Kuhl, K. P.; Hatsukade, T.; Abram, D. N.; Hahn, C.; Chan, K.; Jaramillo, T. F. Trends in the Catalytic Activity of Hydrogen Evolution during CO<sub>2</sub> Electroreduction on Transition Metals. *ACS Catal.* **2018**, *8*, 3035–3040.

(47) Hansen, H. A.; Shi, C.; Lausche, A. C.; Peterson, A. A.; Nørskov, J. K. Bifunctional Alloys for the Electroreduction of CO<sub>2</sub> and CO. *Phys. Chem. Chem. Phys.* **2016**, *18*, 9194–9201.

(48) Sun, K.; Cheng, T.; Wu, L.; Hu, Y.; Zhou, J.; MacLennan, A.; Jiang, Z.; Gao, Y.; Goddard, W. A., III; Wang, Z. Ultrahigh Mass Activity for Carbon Dioxide Reduction Enabled by Gold–Iron Core–Shell Nanoparticles. *J. Am. Chem. Soc.* **2017**, *139*, 15608–15611.

(49) Dinh, C.-T.; Burdyny, T.; Kibria, M. G.; Seifitokaldani, A.; Gabardo, C. M.; García de Arquer, F. P.; Kiani, A.; Edwards, J. P.; De Luna, P.; Bushuyev, O. S.; Zou, C.; Quintero-Bermudez, R.; Pang, Y.; Sinton, D.; Sargent, E. H. CO<sub>2</sub> Electroreduction to Ethylene via Hydroxide-Mediated Copper Catalysis at an Abrupt Interface. *Science* **2018**, *360*, 783–787.

(50) Yoo, J. S.; Christensen, R.; Vegge, T.; Nørskov, J. K.; Studt, F. Theoretical Insight into the Trends that Guide the Electrochemical Reduction of Carbon Dioxide to Formic Acid. *ChemSusChem* **2016**, *9*, 358–363.